Impact Localization in Composite Structures with Deep Neural Networks

Structural Health Monitoring
XX(X):1–12

DOI: 10.1177/14759217241270946
www.sagepub.com/
SAGE

Daniel del-Río-Velilla[1], Andrés Pedraza[1], Antonio Fernández-López[1]

Abstract

This research looks at the application of Deep Neural Networks (DNNs) for low-energy impact localization in composite structures, a key aspect of Structural Health Monitoring in the aerospace sector. The methodology used in this study involves the generation of a consistent impact dataset using an Autonomous Impact Machine, followed by meticulous data processing. The training of the DNN models was focused on minimizing the Euclidean distance between the predicted and actual impact positions employing custom loss functions. This study yielded several significant findings. First, it confirmed the feasibility of using DNNs for effective impact localization in complex composite structures, although with varying degrees of accuracy across different impact locations but with an average error of the same order as the labeling error. Second, it was observed that the performance of the models was considerably influenced by structural features, such as the presence of stringers and the placement of sensors. The architecture demonstrated consistent performance across multiple trained models, indicating their robustness and potential for generalization. The implications of these findings for structural health monitoring are substantial, suggesting that DNNs can be a valuable tool for early damage detection in composite structures.

Keywords

SHM, impact location, low energy impact, CFRP, Deep Neural Network, Artificial Intelligence

Introduction

Composite materials have become a staple in aerospace engineering and have been prized for their impressive specific mechanical properties. Despite their strengths, these materials are vulnerable to low-energy impacts (under 5 J[1]) that can cause various types of damage, such as cracks in the polymer matrix, fiber fractures, or delaminations[2]. The severity and nature of the damage caused by the impact are influenced not only by the energy of the impact, but also by the characteristics of the Impacting Object (IO), such as its mass and velocity[3]. This damage compromises the mechanical integrity of the structure[4–6] and can significantly reduce its useful life due to fatigue[7,8], hence the importance of having the ability to locate an impact received by the structure.

To effectively manage these challenges, Structural Health Monitoring (SHM) plays a critical role[9]. SHM involves a continuous or periodic evaluation of structures to detect and assess damage, enhancing the safety and reliability of aerospace vehicles. Provides a proactive maintenance approach, potentially detecting problems before they become severe. Non-Destructive Inspection (NDI) techniques, such as ultrasound inspection, are a part of SHM strategies[10,11]. These techniques are essential to assess the extent of damage in composite structures. However, NDI methods need to know where a damage is located in order to assess it, which underscores the importance of accurate damage localization in the SHM process.

In the realm of aerospace engineering, the literature presents a diverse range of methodologies to pinpoint impact locations[12,13] on composite structures. Many external aircraft components (such as aerodynamic surfaces and fairings, which have little curvature) are prone to low-energy impacts. A significant portion of these studies focus on flat panels, both with and without stiffeners, as the primary test subjects. To achieve impact localization, researchers have employed various sensing technologies. Piezoelectric sensors are a common choice, as evidenced in several studies[14–17], while others have explored the combined use of accelerometers and fiber optic sensors[18]. These sensors predominantly utilize time-of-arrival techniques, though their application has been largely limited to relatively simplistic structural configurations. Two critical aspects that have attracted attention in this field are the uncertainty associated with the localization of experimental data[19] and the optimization of the placement of the sensor in the test samples[20]. These considerations are vital to enhance the accuracy and efficiency of impact detection systems in composite aerospace structures.

In the field of SHM, traditional damage detection techniques are increasingly being replaced by innovative solutions that utilize Artificial Intelligence (AI) algorithms[21,22]. This change is particularly relevant in the context of composite structures, where the complexities of their geometry

[1]Universidad Politécnica de Madrid, Spain

Corresponding author:
Daniel del-Río-Velilla, Universidad Politécnica de Madrid, Escuela Técnica Superior de Ingeniería Aeronáutica y del Espacio, Edificio A, Laboratorio de química, Plaza del Cardenal Cisneros N3, 28040, Madrid.
Email: daniel.delrio.velilla@upm.es

and laminate stacking sequences pose significant challenges in accurately locating impacts with minimal margins of error.

A growing body of research is focused on harnessing AI for impact localization within composite structures[23–27]. These studies represent pivotal steps toward integrating AI into SHM, yet predominantly feature relatively simplistic structural models, such as untiffened plates. Furthermore, the development of these AI models often relies on simulated data or limited experimental datasets to train supervised learning algorithms. This approach, while valuable, highlights the need for further research employing more complex structures and comprehensive experimental data to fully realize the potential of AI in SHM for composite materials.

In this study, the viability of deep neural networks (DNNs) to locate impacts in composite structures has been developed, a key aspect of SHM. We specifically examine how variations in the training dataset, especially concerning the number and spatial distribution of impact coordinates, affect the model's accuracy. The following approach consists of selecting and instrumenting a specimen, acquiring the data through a Computer Numerical Control (CNC) impactor, processing the acquired data, defining the model, and training them. The results highlight high prediction accuracy and precision, with an average error of 3.47 mm and a standard deviation of 2.3 mm on a stiffened panel of Carbon Fiber Reinforced Polymer (CFRP) of 0.566 m^2 impactable area. These findings are crucial for advancing SHM techniques, particularly for guiding subsequent NDI to assess potential damage after impact.

The paper follows a structured format comprising several key sections. Initially, the materials and methods are delineated, encompassing an exposition of the specimen under investigation, its boundary conditions, the experimental setup, and the methodologies employed for data acquisition and processing. Subsequently, a comprehensive explanation of the DNN model is provided, along with requisite data preprocessing procedures tailored to suit the model's input requirements. Finally, the results obtained are presented, followed by an in-depth discussion aimed at contextualizing and interpreting the findings.

Materials and methods

Description of the Specimen

The specimen selected for this study is a flat CFRP panel. This panel is crafted from unidirectional prepreg, arranged in a quasi-isotropic stacking sequence. Additionally, a T-beam stiffener (previously cured) was bonded to the plate using structural epoxy adhesive. An image of the reinforced CFRP plate is presented in Figure 1a. The dimensions of the plate are $752.3 \times 752.7 \times 2$ mm^3. Its reference system is defined with the X-axis running perpendicular to the stiffener, the Y-axis parallel to it, and the Z-axis forming an orthonormal coordinate set.

To effectively capture the acoustic waves emanating from the impacts, which will be used to feed the DNN models, 7BB-20-3 piezoelectric (PZT) sensors are used. These sensors, which have a circular shape with a diameter of 20 mm, exhibit a resonant frequency of 3.6 kHz and have specified values of impedance and capacitance at $500\ \Omega$ and 20 nF, respectively. A total of eight PZT sensors are integrated into the specimen. Figure 1b illustrates their intended placement on the plate, although there may be slight variations in their actual positions due to manual installation. PZTs are glued to the same surface as the stringer. The signals from these sensors are captured via biaxial cables, which are soldered to each sensor and then connected to a National Instruments NI-USB-6356 data acquisition card, capable of operating at various sampling rates (SRs).

Boundary Conditions and Specimen Setup

The experimental setup begins with the establishment of boundary conditions for the CFRP plate specimen. For this purpose, the plates sides along the Y-axis are rigidly fixed using two 40×40 mm^2 extruded aluminum profiles. In contrast, the sides of the X-axis are left unrestrained, providing a free boundary condition. The plate is secured to the aluminum profiles using clamps, effectively restricting all its degrees of freedom. However, this arrangement slightly reduces the impactable surface area on the X-axis by 40 mm on each side due to the presence of the profiles. The modified impactable area, post-boundary condition application, is shown in Figure 2.

Composition of the Impact Database

The primary objective of this study is to assess the capability of DNNs in accurately identifying locations of multi-energetic real impacts. To achieve this, a robust and detailed impact database is crucial. This database serves as the foundational training set for DNN models, enabling them to learn and interpret the underlying physics of impacts.

The database comprises a series of impacts on the specimen, carried out by dropping a specially designed IO from predetermined heights, a process which constitutes a free-fall scenario. This IO, which has different mass configurations, is released from different heights to vary the impact velocities. The ability to control these impact velocities is critical for simulating a diverse range of real-world impact conditions. This variability is fundamental for DNN models, enabling them to accurately predict a spectrum of parameters associated with various impact scenarios.

The IO, as illustrated in Figure 3, features a tubular body with an impact tip mounted at the bottom. Steel discs can be added or removed from its central compartment to adjust its mass according to the requirements of the experiment. The upper section of the IO is capped with an iron part, which serves a dual purpose. First, it secures the steel discs inside the body. Second, and most crucially, it allows for the attachment of the electromagnet, which will pick it up to raise it to the defined release height. This electromagnet attachment is pivotal in achieving precise control over the IO's release height, thereby ensuring the accuracy and repeatability of the impacts during the experimentation phase.

In the context of the Composition of the Impact Database subsection, it is essential to detail the methodologies employed for both spatial and energetic discretization. These processes are essential to ensure that the impact data captured is comprehensive and representative of a wide range of

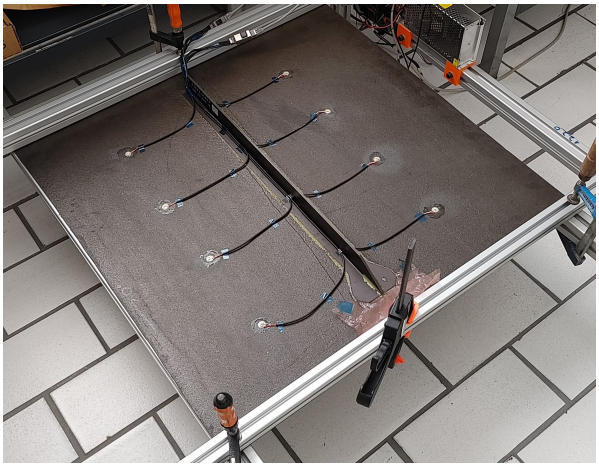

(a) Photograph of the specimen showcasing the integrated sensors.

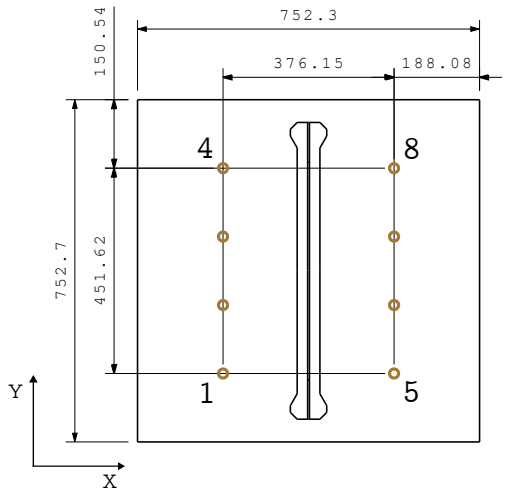

(b) Schematic layout of the specimen, values in mm.

Figure 1. Visual documentation of the specimen employed in the research.

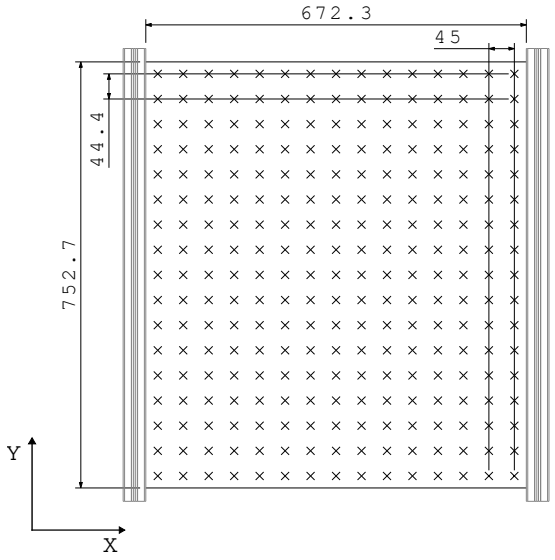

Figure 2. Illustration of the impact coordinate grid on the specimen, values in mm.

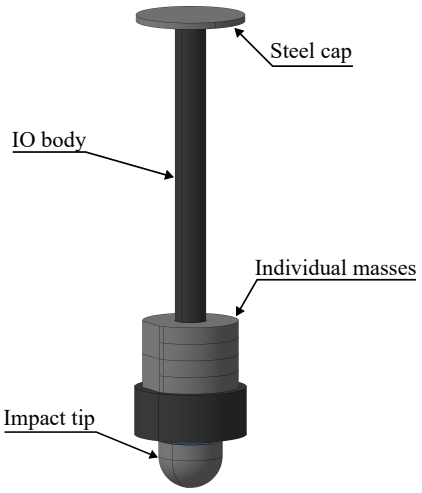

Figure 3. Impactor Object description.

scenarios, thereby facilitating effective training of the NNs. We will explore these two key aspects as follows:

- *Spatial discretization*: this process involves dividing the surface of the plate into a grid with predetermined impact coordinates. This grid results from intersecting the spatial discretizations of the X and Y axes. The distance between two coordinates should be greater than the tube diameter (42.3 mm) through which the IO falls. Therefore, taking into account the dimensions shown in Figure 2, a mesh of $\mathrm{N}_x = 15$ by $\mathrm{N}_y = 17$ with a total of 255 coordinates is obtained.
- *Energetic Discretization*: it involves creating a dataset with impacts with multiple masses, velocities, and energies. This is achieved by adjusting the IO's mass and altering its release height for different impact velocities. The relationship between release height and impact velocity is derived from the principles of kinetic and potential energy. Equating these energy expressions enables the calculation of impact velocity,

$$\frac{1}{2}mv^2 = mgh \quad \rightarrow \quad v = \sqrt{2\mathrm{g}h} \quad \left[\frac{\mathrm{m}}{\mathrm{s}}\right], \qquad (1)$$

where m is the mass of the IO, v is the velocity of the IO when impacting the panel, g is the gravity constant, and h is the release height where the IO is dropped. Furthermore, this study aims to demonstrate that the position of two impacts with the same energy level but with different combinations of IO mass and release height can be discerned,

$$\begin{cases} E_{p,1} = m_1 g h_1 \\ E_{p,2} = m_2 g h_2 \end{cases} \rightarrow \quad \frac{m_1}{m_2} = \frac{h_2}{h_1}, \qquad (2)$$

being $E_{p,1}$ and $E_{p,2}$ the same potential energy value. This concept is visually represented in Figure 4, which shows an energy heat map with equi-energetic lines. These visualizations aid in understanding the relationship between mass, height, and energy, which is particularly relevant in the context of low-energy impacts. The different combinations of energy have

been achieved with five masses from 60 to 260 g with 50 g jumps and ten heights from 35 to 260 mm with 25 mm jumps. The minimum and maximum impact energy levels applied to the tests have been 20.6 and 663.2 mJ, respectively. These combinations of mass and release height of the realized impacts are also shown as dots in Figure 4. It can be seen that several of the impacts performed comply with Equation (2) as multiple points are under the same equi-energetic line.

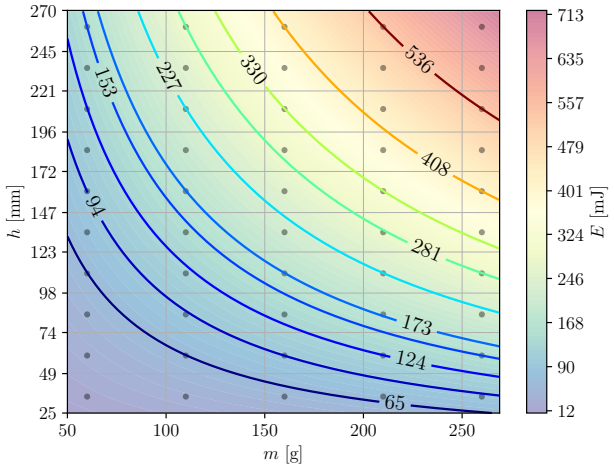

Figure 4. Energy map with equi-energetic lines and the combinations of mass and release height of the realized impacts represented by dots.

All impacts performed have remained below the minimum energy value necessary to generate damage to the structure. Thus, a dataset has been acquired in which the studied structure has remained unchanged.

Each combination of coordinates, mass, and height was tested multiple times, resulting in a comprehensive data set of experimental impacts 40 460. However, after accounting for data acquisition errors explained in Subsection *Data Preprocessing for Deep Neural Network Training*, the final count of accurately captured and labeled impacts is 37 898.

Acquisition of Experimental Impacts

The reliability and precision of the data fed into AI models are crucial, especially when experimental data are used for training. Inaccuracies in the impact data, such as mislabeled coordinates, can lead to erroneous interpretations of the underlying physics of the model. Due to the critical need for consistent and accurate impact data, an Autonomous Impact Machine (AIM) has been developed, depicted in Figure 5. The AIM is a CNC-based machine designed to eliminate the variability and potential errors associated with manual impact testing. This machine ensures high repeatability and reliability in the impact dataset.

The AIM boasts a capable operational volume of $1440 \times 990 \times 150$ mm^3, accommodating the previously described IO with a maximum mass of 1 kg and a maximum release height of 2 meters, resulting in an impact energy of up to 19.62 J (although the study was carried out with much lower energy). The machine operates by raising the IO to a predetermined height using an electromagnet and then

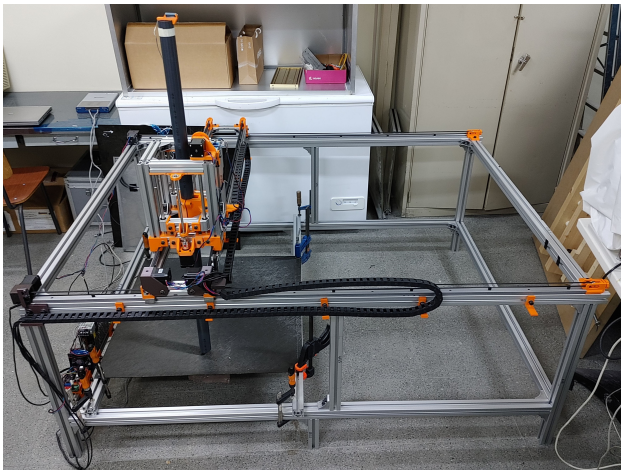

Figure 5. Autonomous Impact Machine.

releasing it in free fall. The IO descends through a guiding tube positioned at pre-defined impact coordinates, ensuring precise impact locations.

The reason for using AIM to acquire real impacts versus generating a database of impacts using simulation methods is primarily the high computational cost required to simulate impacts on complex structures. If simulations are performed using the Ray Tracing method, impacts can be generated at a rate of 0.29 samples per minute, which would be reduced to 0.004 if generated using a finite element method[28]. AIM has achieved a rate of 3 samples per minute, 10 and 750 times faster than the other two methods.

Controlled by an Arduino Mega 2560 with an added Ramps 1.4 power board, the AIM's operations are orchestrated via a MATLAB script. This program not only controls the AIM's movements and IO releases but also manages the acquisition of acoustic waves through the NI-USB-6356 acquisition card. Figure 6 shows an impact measurement acquired by the procedure described above. This figure shows the variation of the voltage acquired by each sensor during the one-second acquisition window.

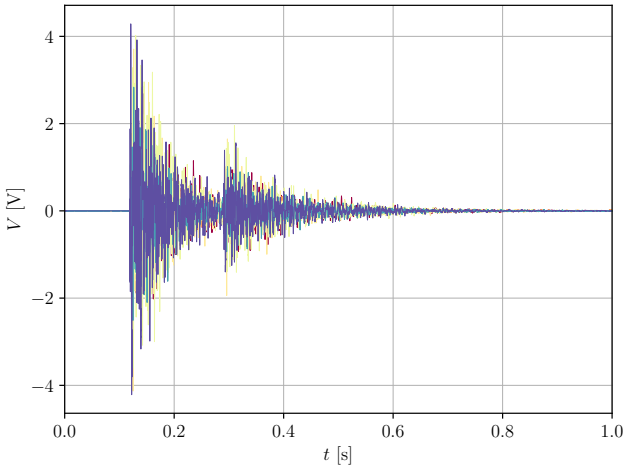

Figure 6. Example of the raw signal of an impact acquired by the eight PZTs glued on the specimen.

Each impact performed by the AIM generates eight time series corresponding to the eight PZT sensors. The raw impact acquisition is performed for one second with the

maximum SR allowed by the NI-USB-6356 card, 2 MHz per channel. This acquired signal amounts to a substantial 16 million sampling points per impact. Such a large volume of data exceeds the processing capabilities of most DNN models, and much of the signal has no useful information for the location task.

To avoid this excess of data, the duration of the impact was reduced to 16 ms, thus eliminating a large amount of signal but maintaining the information that can provide the DNN with the damping of the impact. It can be seen in Figure 9 that at this signal length the sensors pick up the damping mentioned above. The SR has also been reduced from 2 MHz to 125 kHz so that the input of the model ends up as a $8 \times 2\,000$ array per impact, a manageable size for the DNN architecture and hardware used (NVIDIA GeForce RTX 4070) and with good signal quality.

The starting point for each impact is identified 20 sampling points before the first sensor's reading exceeds a threshold of 5 mV, and the data window is closed 2 000 sampling points later. After that, each impact is labeled with relevant parameters, such as coordinates (X, Y), IO mass and release height.

However, it is important to acknowledge that the actual values are subject to tolerances related to the AIM and IO hardware. The maximum error in impact coordinate position labeling,

$$\delta = \pm \left(\rho_t - \rho_{IO} + \frac{\phi_{tip}}{2} \right)$$

combines the tolerance between the drop tube and the IO along with the IO tip diameter, where $\rho_p = 17.8$ mm is the radius of the drop tube, $\rho_{IO} = 17.5$ mm is the radius of the IO and $\phi_{tip} = 1$ mm is the diameter of the IO tip contact area. Hence, the absolute maximum labeling error, ε, of the variables X and Y is,

$$\varepsilon = |\delta| = 0.8 \text{ mm}. \tag{3}$$

To obtain the Euclidean deviation of the coordinate labeling, ε_Δ, the norm of both axis errors needs to be performed,

$$\varepsilon_\Delta = \sqrt{\varepsilon_X^2 + \varepsilon_Y^2} = 1.13 \text{ mm}. \tag{4}$$

In summary, the AIM plays a pivotal role in ensuring the integrity and consistency of the impact data, forming the backbone of our experimental setup to train accurate and reliable DNN models.

Neural Network

Data Preprocessing for Deep Neural Network Training

Before data is fed into the DNN, a critical stage of data preprocessing is required. This stage ensures the quality and relevance of the data derived from the AIM, facilitating effective learning by the DNN.

The first step is to check that all impacts have been acquired and stored correctly. To verify that the onset of impact was detected correctly to trim it, the Root Mean Square Value (RMSV) of each sensor was calculated. If the RMSV falls below 0.1 volts, it indicates that the sensor did not adequately capture the impact beginning and only saved noise, as shown in Figure 7a. Furthermore, if any of the initial 200 samples of an impact do not exceed 0.05 volts, it indicates a false trigger, which leads to the rejection of that impact from the dataset, as depicted in Figure 7b.

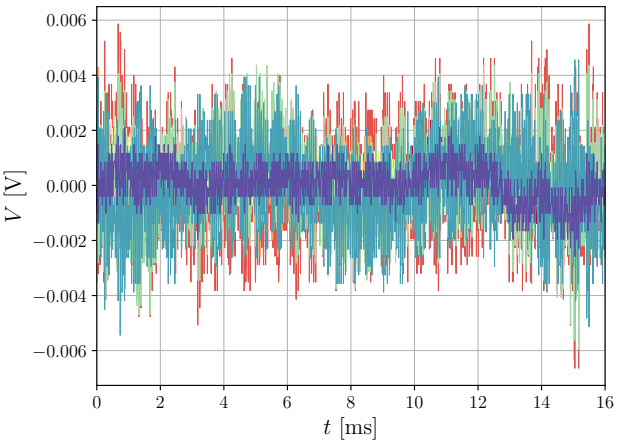

(a) Impact with a RMSV lower than 0.1 V.

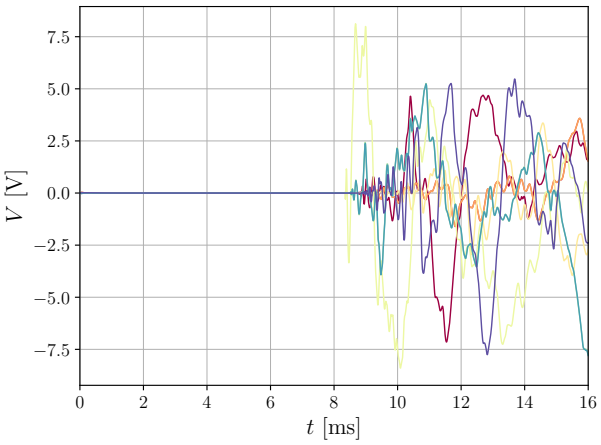

(b) Impact with false trigger indication.

Figure 7. Examples of signals acquired by PZTs glued on the specimen of impacts with data quality issues.

A correlation matrix is computed for the sensors based on a randomly selected impact sample, as shown in Figure 8. This matrix provides insight into the similarity of the data across different sensors. If the correlation value is 1, it indicates that the signals are the same; on the other hand, if the value is 0, the signals are not similar at all. In this specific case, it reveals that sensors 2-3 and 6-7 have highly similar readings, suggesting an issue with data acquisition in these pairs. Consequently, data from these sensors will be excluded from result analysis in this study.

Once the database has been cleaned of erroneous impacts and prior to training the DNN, it is essential to organize the generated dataset into three distinct sets: training, validation, and testing. Each impact is assigned exclusively to one of these groups to ensure the robustness of the training process and the accuracy of the model evaluation.

- *Training Set:* This set includes impacts directly used in training the DNN model. It constitutes 60% of the total dataset.
- *Validation Set:* The validation set is used to monitor and validate the training process. Although this set

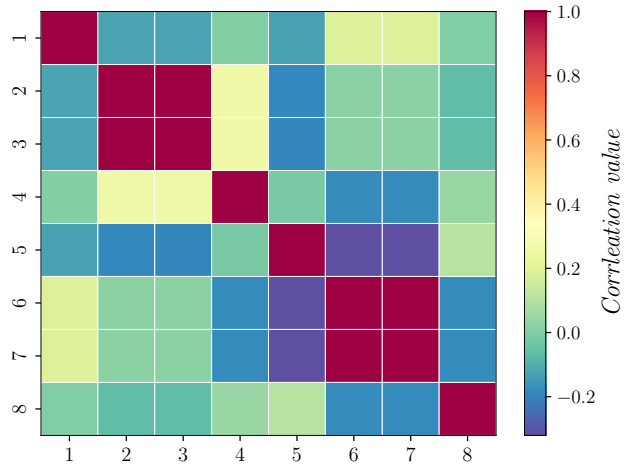

Figure 8. Sensor correlation matrix for an impact.

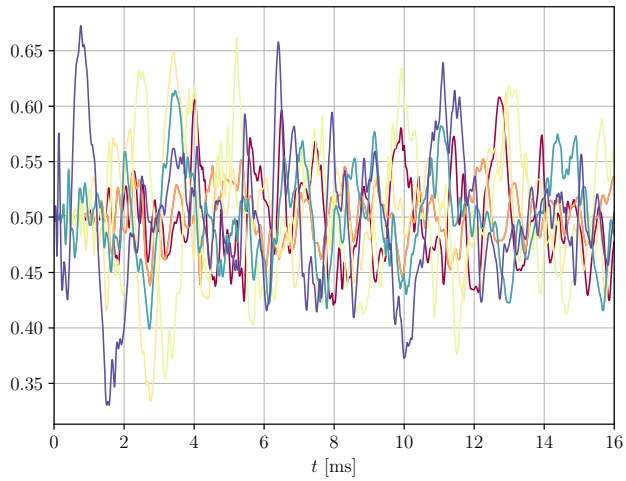

Figure 9. Example of the signals acquired by PZTs attached to the specimen of an impact after being processed and prepared for DNN training.

does not directly contribute to the learning process, it helps in tuning the model parameters and prevent over fitting. It comprises 20% of the dataset.

- *Testing Set:* This set is crucial as it includes impacts that are completely unseen by the model during training. It is used to evaluate the model's performance and generalization capabilities. It is composed of the remaining 20% of the impacts of the dataset.

Normalization is applied to all impacts to scale the data and labels, ensuring uniformity in the range of values fed into the network. The normalization is defined as

$$\hat{x} = \frac{x - \min(x)}{\max(x) - \min(x)}. \tag{5}$$

In this equation, x represents the matrix containing all impacts or an array of all labels for a single variable to normalize, and $\hat{x}$ is the normalized label. This scaling limits the values between 0 and 1, addressing potential issues during training caused by wide-ranging input values. Importantly, the maximum and minimum values used in the normalization formula are derived from the training set and then applied consistently across all groups.

Figure 9 illustrates a typical processed and prepared impact, ready to be entered into the DNN.

This structured approach to data preparation is vital for effective DNN training and evaluation, ensuring that the model is well-equipped to handle real-world data and deliver accurate predictions.

Deep Neural Network Architecture

The DNN models in this research were developed using the PyTorch framework, a choice driven by its flexibility and robustness in handling complex NN architectures.

A conceptual diagram of the DNN architecture is presented in Figure 10. This architecture is divided into two primary stages: the Feature Extraction Stage (FES) and the Regression Stage (RS). The FES, represented by orange blocks in the diagram, compresses the acoustic wave data from the PZTs sensors into a compact feature array. This stage is crucial to distill the most significant characteristics from the raw impact data. The output of this stage is then fed into the RS, depicted in green blocks. In RS, independent regressions are performed on the extracted features to predict various impact parameters, producing an array of dimensions with the same number of elements as the parameters predicted by the model.

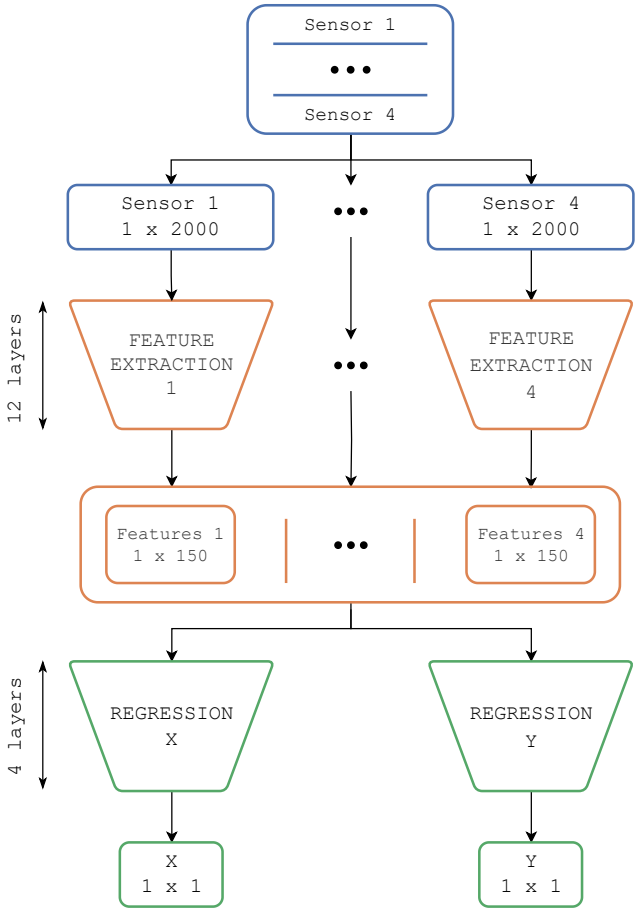

Figure 10. Diagram of the Deep Neural Network architecture.

Delving deeper into the architecture, both FES and RS consist of a Multilayer Perceptron, with each subsequent layer having fewer neurons than its predecessor, like an

encoder configuration. Figure 11 illustrates the internal structure of these stages. Each miniblock within these stages (shown in light gray) comprises a dense linear layer, a dropout layer that randomly deactivates 5% neurons during training to prevent overfitting, and a hyperbolic tangent (tanh) activation function.

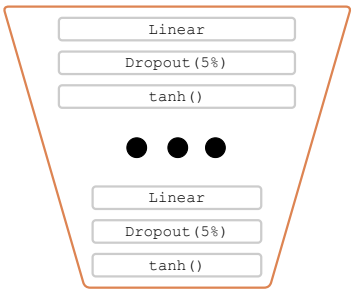

Figure 11. Detailed view of the individual layers within a block.

A matrix of size 4×2000 is introduced that contains the first 2000 time stamps of the impact acquired by the four selected sensors. This matrix is separated into four 1×2000 arrays to enter the FES stage, each array in one block. FES compresses the information for each impact, reducing the number of neurons per layer, until a latent feature array of size 1×150 is generated. The process of extracting features from signals consists of the signal processed by a succession of layers in which the number of neurons is progressively reduced. In this way, the signal is compressed by extracting the most representative characteristics of the signal. The output of each FES is concatenated until a latent vector of 1×600 is obtained, which combines all information from the four sensors. This latent vector is fed into the RS blocks to finally return the X and Y coordinates of the impact.

A detailed description of the Feature Extraction and Regression blocks is presented in Tables 1 and 2.

Table 1. Feature Extraction block layers.

Layer	Num. neurons	Act. funct.	Dropout [%]
1	1800	tanh	5
2	1650	tanh	5
3	1500	tanh	5
4	1350	tanh	5
5	1200	tanh	5
6	1050	tanh	5
7	900	tanh	5
8	750	tanh	5
9	600	tanh	5
10	450	tanh	5
11	300	tanh	5
12	150	tanh	5

Table 2. Regression block layers.

Layer	Num. neurons	Act. funct.	Dropout [%]
1	450	tanh	5
2	300	tanh	5
3	150	tanh	5
4	1	tanh	0

Training Process of Deep Neural Network Models

Training DNN models requires careful selection of a loss function and an optimization algorithm. The loss function quantifies the discrepancy between the model's predictions and the actual values, while the optimizer utilizes this information to adjust the model's parameters, thereby enhancing its performance. Synergy between the loss function and the optimizer is crucial for the effective training of DNNs.

For this study, a tailored loss function was devised, aiming to predict the impact position rather than treating the X and Y coordinates independently. The loss function is defined as the Euclidean distance between the predicted and actual impact positions,

$$loss = \sqrt{(\hat{y}_0 - y_0)^2 + (\hat{y}_1 - y_1)^2}. \quad (6)$$

Here, y represents the normalized labels for the impact position (with y_0 and y_1 being the X and Y coordinates, respectively), and $\hat{y}$ denotes the predicted coordinates. Training was carried out in batches of 32 impacts, with the loss in the batch calculated as the mean of the losses of each impact within the batch, thus reducing the impact of potential outliers.

The optimizer chosen to minimize this loss is Adam, a standard option within the PyTorch framework. The training regimen encompassed various combinations of epochs (e) and learning rates (lr). This training method avoids falling into local minimums by abruptly changing lr. The number of epochs indicates how many times the entire training and validation datasets are passed through the learning algorithm. The learning rate is a hyperparameter controlling the extent to which the model's weights are updated during training. The parameters used for each training step are detailed in Table 3.

Table 3. Parameters used to train each model.

Parameter	Step					
	1	2	3	4	5	6
e	40	30	20	20	20	20
$\log_{10}(lr)$	-5	-6	-7	-5	-6	-7

In addition, a weight decay parameter set to 10^{-5} was implemented as part of the training strategy. Weight decay serves as a regularization method to prevent overfitting, ensuring that the model generalizes well to new, unseen data and does not merely memorize the training set.

This specific training configuration was applied uniformly across all models developed in this research. Figure 12 provides an illustration of a model training process, displaying the progress of the average loss (the cumulative batch losses divided by the total number of impacts) at the end of each epoch of both training and validation datasets.

This structured approach to train the DNNs ensures that the models are not only accurate, but also robust and capable of generalizing well to different impact scenarios.

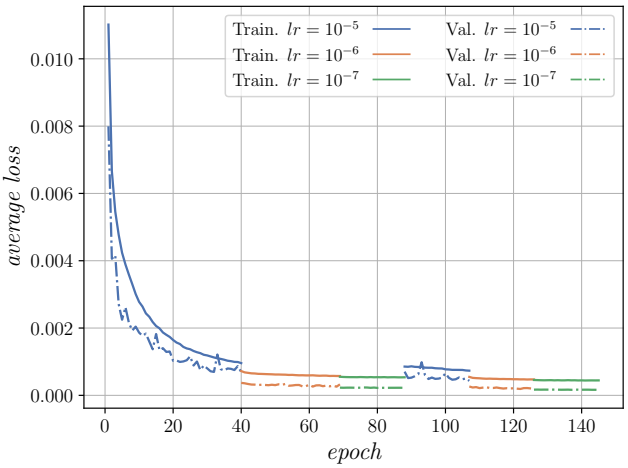

Figure 12. An example of the training process demonstrating loss reduction over epochs.

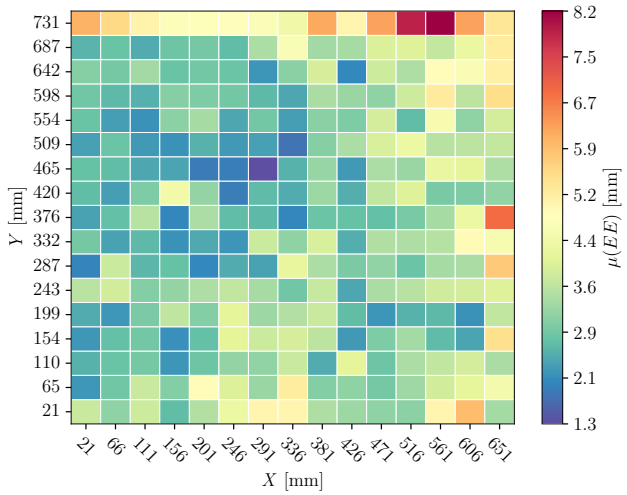

(a) Average *EE*.

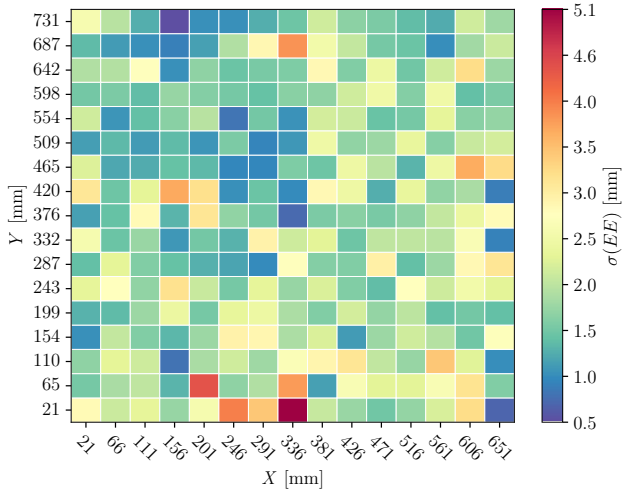

(b) Standard deviation *EE*.

Figure 13. Heatmaps of test dataset predictions for best performance model.

Results

Evaluation Metric for Regressive Models

The performance of the models in this study, which act as regressors, cannot be gauged using typical metrics such as confusion matrices applicable to classifiers. Instead, the models are assessed by using the Euclidean distance of the Error,

$$EE = \sqrt{(x_p - x_l)^2 + (y_p - y_l)^2} \quad [\text{mm}], \qquad (7)$$

where x and y are the coordinates, and the sub index p and l referee to predicted or labeled value. This metric is particularly relevant, as it considers the combination of the two model outputs, the X and Y coordinate predictions, to evaluate the accuracy of the impact location.

To evaluate the performance of the architecture defined in Figure 10 in impact location, four different random distributions of samples have been created in the training, validation, and test sets. With these four sets, four models have been trained. This approach allows for k-fold validation, which provides a more comprehensive assessment of the performance of the average model in various data distributions. This reduces the impact, both negative and positive, that an outlier can have on the final metrics.

Case Study 1: Feasibility of Impact Location

The primary objective was to determine the feasibility of using DNN for equi-energetic impact location in composite structures whose geometry is representative in the aerospace sector.

Figure 13 illustrates the performance of the model with the lowest EE average. In these subfigures, we want to check that the EE is homogeneous in all impact coordinates, so each grid cell represents an impact coordinate, and its color refers to an EE metric for that particular cell. Thus, Subfigure 13a shows the mean EE, and Subfigure 13b shows the standard deviation of EE.

A detailed analysis, Figure 14, reveals that the higher mean error at the coordinates $\mathrm{Y} = 731$ mm is due to the prediction set being significantly offset from the target. Despite this offset, the low standard deviation indicates high precision, albeit with lower accuracy.

In contrast, the predictions at $[\mathrm{X}, \mathrm{Y}] = [336.6, 376.6]$ mm, Figure 15, show a concentration around the target coordinate, indicative of high accuracy and precision.

For a broader view of the model's global localization performance, Figure 16 presents a normalized histogram of EE predictions along with the probability distribution function (PDF) and the cumulative density function (CDF) of the Generalized Extreme distribution. Predictions that exceeded the 99^{th} percentile of the CDF curve were considered outliers and excluded from the analysis results.

Table 4 summarizes the performance metrics for the four models.

Table 4. Performance metrics for the trained models.

Model [*k*]	$\mu(EE)$ [mm]	$\sigma(EE)$ [mm]
1	3.54	2.29
2	3.37	2.29
3	3.50	2.25
4	3.47	2.38
Average	3.47	2.30

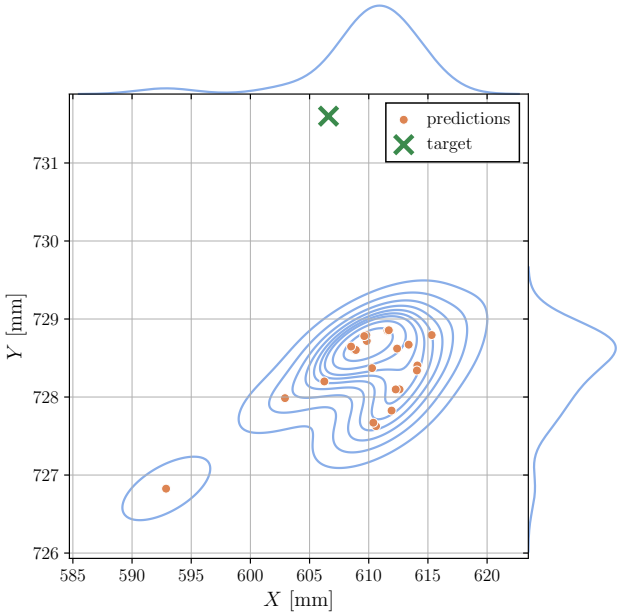

Figure 14. Predictions at [X, Y] = [561.6, 731.6] mm by fold one model.

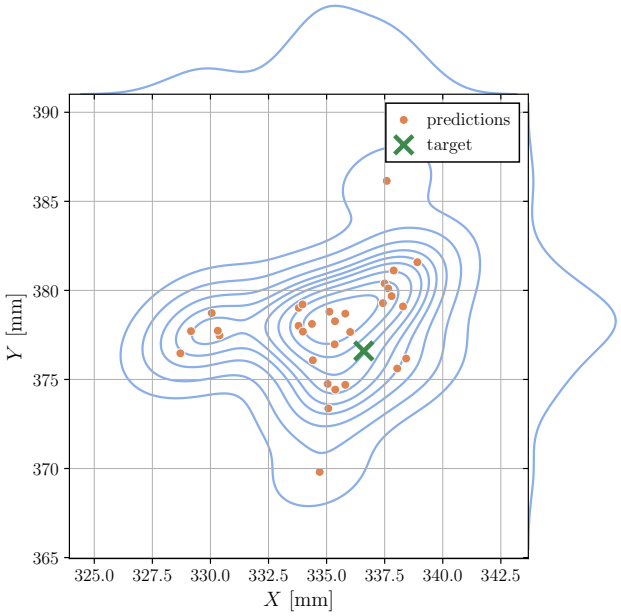

Figure 15. Predictions at [X, Y] = [336.6, 376.6] mm by fold one model.

Case Study 2: Impact of Sensor Distance on Model Performance

This case examines the impact of the distance from the data set impact coordinates to the sensors to assess the sensitivity of the models to this parameter.

A total of 25 subsets of the 3×3 coordinates were analyzed, excluding the $Y = 21$ mm and $Y = 731$ mm coordinates to achieve a square grid and maintain continuity between the subsets. Figure 17 shows the subsets studied in a grid. The label on the X and Y axes refers to the subset index, and the color of each cell indicates the average distance between the impact coordinates and the sensors of that subset.

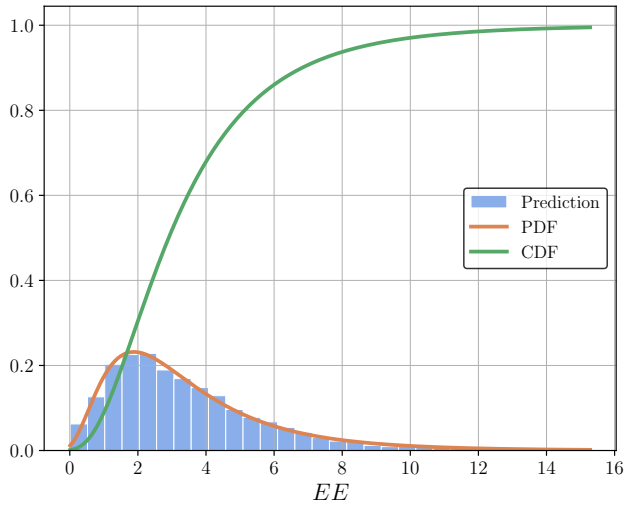

Figure 16. Histogram, PDF, and CDF of *EE* for fold one model.

Figure 17. Average distance in mm from subsets to sensors.

For this case, four models have been trained from each of the established subsets. As in the previous case, the performance of the models has been evaluated with the test data and the average results of each subset (average of the four trained models) are presented in Figure 18.

In particular, there is a consistent error pattern in the X coordinate across subsets, while the errors on the Y axis increase considerably in the $X = 3$ subset, influencing the overall EE.

The increased Y coordinate prediction error, especially in the $X = 3$ subset, becomes more apparent when examining its standard deviation, shown in Figure 19. The correlation between mean error, standard deviation, and distance to the sensors is clearly visible in Figure 20.

These findings highlight the impact of sensor placement and structural features, such as stringers (located in $x = 3$), on the accuracy and precision of DNN-based impact localization in composite structures.

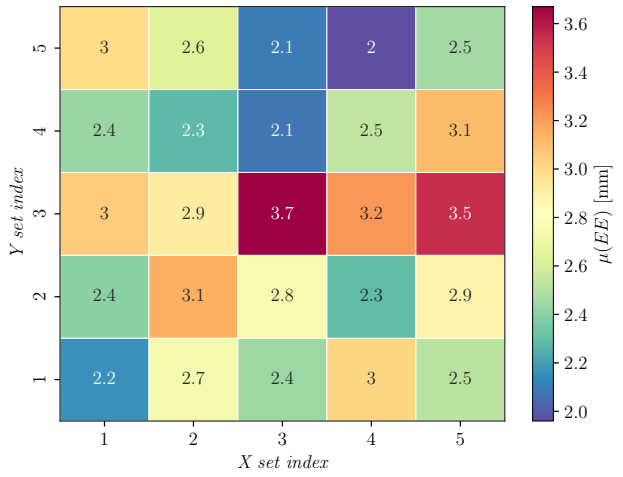

(a) Average X coordinate error.

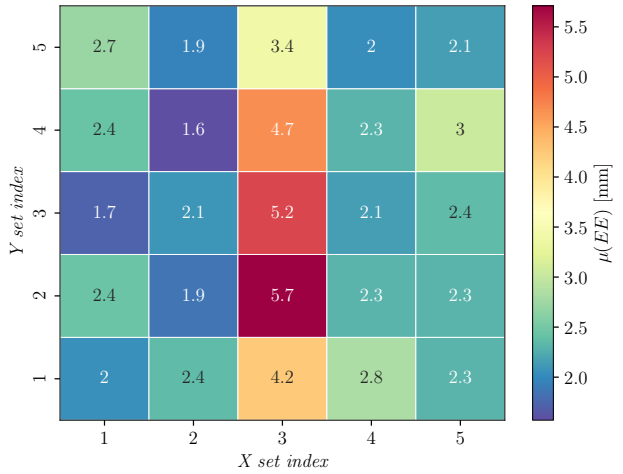

(b) Average Y coordinate error.

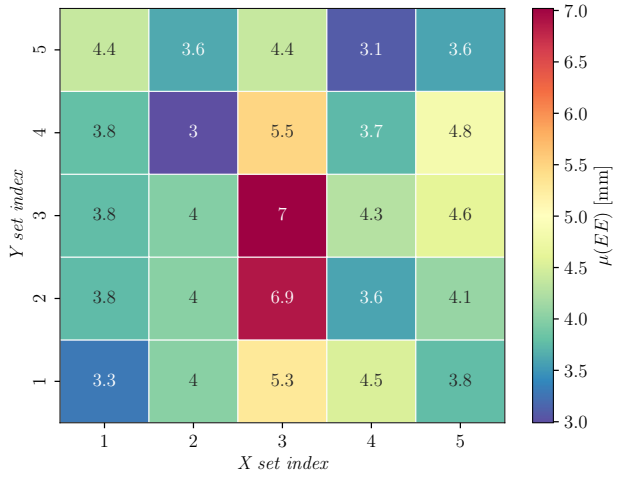

(c) Average *EE*.

Figure 18. Error analysis for subsets.

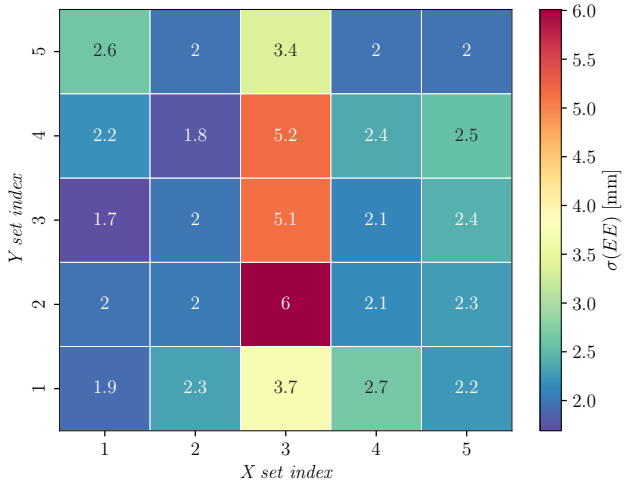

Figure 19. Standard deviation of Y prediction error.

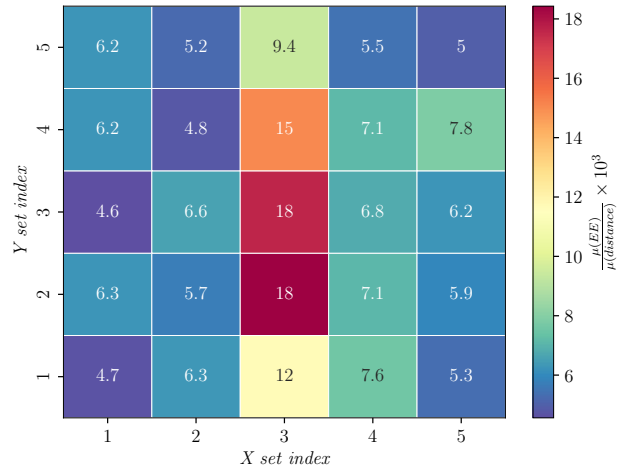

(a) Mean error vs. average distance.

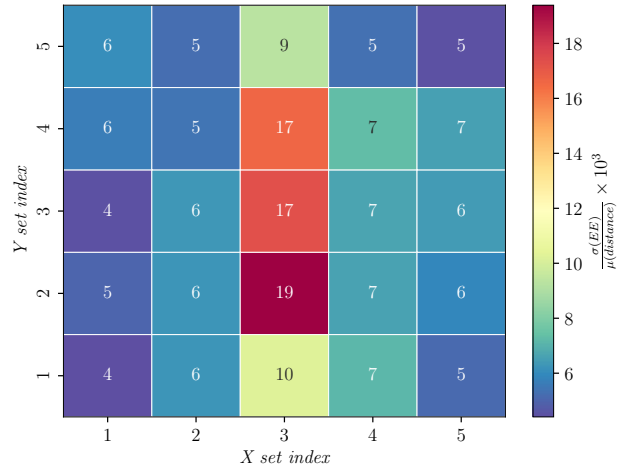

(b) Standard deviation vs. average distance.

Figure 20. Error correlation with distance to sensors.

Discussion

The comprehensive study presented here demonstrates the efficacy of DNN in localizing impacts on composite structures. The results, derived from a methodical approach that includes data preparation, model training, and evaluation, reveal key insights and implications for the application of DNNs in SHM.

The first case study validates the feasibility of using DNNs for equi-energetic impact locating in complex composite structures. Models, trained on a real impact dataset, have shown a promising ability to predict the location of impacts with reasonable accuracy, with an average EE (3.47 mm) of the same order of magnitude as the maximum labeled error

(1.13 mm) on a square plate of side length 752 mm. The use of a custom loss function, defined as the Euclidean distance between predicted and actual impact positions, effectively guided the models to focus on accurate localization. The results from the lowest average Euclidean distance error models indicate a notable variance in prediction accuracy across different impact coordinates, highlighting the model's sensitivity to spatial factors.

The second case study delves into the impact of sensor placement and structural features on the model's performance. The variation in error between different subsets of impact coordinates underscores the influence of physical attributes of the composite structure, such as the presence of stiffeners, and not as much the average distance between sensors and impact coordinates. In particular, the increase in the Y-coordinate predictions in certain subsets is consistent with these structural features, suggesting that the physical layout of the structure plays a significant role in the predictive capacity of the model.

Across different training iterations and k-fold validations, the models exhibited consistent performance, suggesting robustness and a degree of generalization in their predictive capacity. However, the performance variations across different subsets of data also point to the need for diverse and comprehensive training datasets that adequately represent the range of possible impact scenarios and structural variations.

The findings of this study have significant implications for Structural Health Monitoring, particularly in composite materials. The ability of DNNs to accurately localize impacts can be decisive in early damage detection and prevention, potentially leading to improved structural safety and durability. However, the study also highlights the importance of considering structural features and sensor placement in the design of DNN-based monitoring systems.

Future research could focus on enhancing the model's accuracy and generalization by incorporating a wider variety of impact scenarios and structural variations in the training process. Exploring the integration of other types of sensors and data fusion techniques may further improve the robustness of impact localization models. The influence of environmental factors, such as temperature and humidity, on the model's performance is another area worth investigating. This study also opens the door to try to predict impact energy using DNNs. The combination of impact locator models and energy characterizers would be a breakthrough in damage location capabilities for complex aircraft structures.

In conclusion, this study establishes the potential of Deep Neural Networks in the field of impact localization on composite structures, paving the way for more advanced and reliable structural health monitoring systems. Nuanced understanding of factors affecting model performance can guide the development of more sophisticated and accurate monitoring solutions in the future.

Acknowledgements

This project has received funding from the National Research Program Retos de la Sociedad under the Project STARGATE: Desarrollo de un sistema de monitorización estructural basado en un microinterrogador y redes neuronales (reference PID2019-105293RB-C21)

Declaration of conflicting interests

The author(s) declared no potential conflicts of interest with respect to the research, authorship, and/or publication of this article.

References

1. Mittelman A. Low-energy repetitive impact in carbon-epoxy composite. *Journal of Materials Science* 1992; 27: 2458–2462. DOI:10.1007/BF01105058/METRICS. URL https://link.springer.com/article/10.1007/BF01105058.
2. Davies GAO and Olsson R. Impact on composite structures. *THE AERONAUTICAL JOURNAL* 2004; : 541–563DOI:10.1017/s0001924000000385.
3. Aryal B, Morozov EV, Wang H et al. Effects of impact energy, velocity, and impactor mass on the damage induced in composite laminates and sandwich panels. *Composite Structures* 2019; 226. DOI:10.1016/J.COMPSTRUCT.2019.111284.
4. Pavier MJ and Clarke MP. Experimental techniques for the investigation of the effects of impact damage on carbon-fibre composites. *Composites Science and Technology* 1995; 55: 157–169. DOI:10.1016/0266-3538(95)00097-6.
5. Corum JM, Battiste RL and Ruggles-Wrenn MB. Low-energy impact effects on candidate automotive structural composites. *Composites Science and Technology* 2003; 63: 755–769. DOI:10.1016/S0266-3538(02)00265-8.
6. Zabala H, Aretxabaleta L, Castillo G et al. Impact velocity effect on the delamination of woven carbon-epoxy plates subjected to low-velocity equienergetic impact loads. *Composites Science and Technology* 2014; 94: 48–53. DOI:10.1016/J.COMPSCITECH.2014.01.016.
7. Tai NH, Yip MC and Lin JL. Effects of low-energy impact on the fatigue behavior of carbon/epoxy composites. *Composites Science and Technology* 1998; 58: 1–8. DOI:10.1016/S0266-3538(97)00075-4.
8. Batra RC, Gopinath G and Zheng JQ. Damage and failure in low energy impact of fiber-reinforced polymeric composite laminates. *Composite Structures* 2012; 94: 540–547. DOI:10.1016/J.COMPSTRUCT.2011.08.015.
9. de Medeiros R, Vandepitte D and Tita V. Structural health monitoring for impact damaged composite: a new methodology based on a combination of techniques. *https://doiorg/101177/1475921716688442* 2017; 17: 185–200. DOI:10.1177/1475921716688442. URL https://journals.sagepub.com/doi/abs/10.1177/1475921716688442.
10. Scott I and Scala C. A review of non-destructive testing of composite materials. *NDT International* 1982; 15: 75–86. DOI:10.1016/0308-9126(82)90001-3.
11. Boopathy G, Surendar G, Anand TPP et al. Review on non-destructive testing of composite materials in aircraft applications. *International Journal of Mechanical Engineering and Technology* 2017; 8: 1334–1342.
12. Francesco C, Meo M and Barbieri E. Impact localization in composite structures of arbitrary cross section. *Structural Health Monitoring* 2012; 1: 643–655.
13. Zhong Y, Yuan S and Qiu L. An improved two-dimensional multiple signal classification approach for impact localization on a composite structure. *http://dxdoiorg/101177/1475921715591872* 2015; 14:

385–401. DOI:10.1177/1475921715591872. URL https://journals.sagepub.com/doi/abs/10.1177/1475921715591872.

14. Zhou J, Mathews VJ and Adams DO. Acoustic emission–based impact location estimation on composite structures. *https://doiorg/101177/1475921718820521* 2019; 18: 1652–1668. DOI:10.1177/1475921718820521.
15. Guyomar D, Lallart M, Monnier T et al. Passive impact location estimation using piezoelectric sensors. *Structural Health Monitoring* 2009; 8: 357–367. DOI:10.1177/1475921709102090.
16. Diamanti K, Hodgkinson JM and Soutis C. Detection of low-velocity impact damage in composite plates using lamb waves. *Structural Health Monitoring* 2004; 3: 33–41. DOI:10.1177/1475921704041869.
17. Zhou J, Mathews VJ and Adams DO. Acoustic emission–based impact location estimation on composite structures. *https://doiorg/101177/1475921718820521* 2019; 18: 1652–1668. DOI:10.1177/1475921718820521. URL https://journals.sagepub.com/doi/abs/10.1177/1475921718820521.
18. Frieden J, Cugnoni J, Botsis J et al. Low energy impact damage monitoring of composites using dynamic strain signals from fbg sensors - part i: Impact detection and localization. *Composite Structures* 2012; 94: 438–445. DOI:10.1016/J.COMPSTRUCT.2011.08.003.
19. Seno AH and Aliabadi MF. Uncertainty quantification for impact location and force estimation in composite structures. *Structural Health Monitoring* 2022; 21: 1061–1075. DOI:10.1177/14759217211020255.
20. Pearson MR, Eaton M, Featherston C et al. Improved acoustic emission source location during fatigue and impact events in metallic and composite structures. *Structural Health Monitoring* 2017; 16: 382–399. DOI:10.1177/1475921716672206.
21. Malekloo A, Ozer E, AlHamaydeh M et al. Machine learning and structural health monitoring overview with emerging technology and high-dimensional data source highlights. *Structural Health Monitoring* 2022; 21: 1906–1955. DOI:10.1177/14759217211036880.
22. Su Z and Ye L. Quantitative damage prediction for composite laminates based on wave propagation and artificial neural networks. *Structural Health Monitoring* 2005; 4: 57–66. DOI:10.1177/1475921705049747.
23. Tabian I, Fu H and Khodaei ZS. Impact detection on composite plates based on convolution neural network. *Key Engineering Materials* 2019; 827: 476–481. DOI:10.4028/www.scientific.net/KEM.827.476.
24. Cuomo S, Simone MED, Andreades C et al. Machine learning for impact detection on composite structures. *Materials Today: Proceedings* 2021; 34: 93–98. DOI:10.1016/j.matpr.2020.01.295.
25. Yu H, Seno AH, Khodaei ZS et al. Structural health monitoring impact classification method based on bayesian neural network. *Polymers* 2022; 14: 3947. DOI:10.3390/polym14193947.
26. Balasubramanian P, Kaushik V, Altamimi SY et al. Comparison of neural networks based on accuracy and robustness in identifying impact location for structural health monitoring applications. *Structural Health Monitoring* 2023; 22: 417–432. DOI:10.1177/14759217221098569.
27. Chen Z, Zhu H, Wu J et al. Stress–strain-based crack damage detection of composite structures using selective kernel convolutional networks and continuous wavelet transform. *Structural Health Monitoring* 2022; : 147592172211344DOI:10.1177/14759217221134452.
28. Iglesias FS, Serrano AG, Rodriguez AP et al. Validation of a ray-tracing-based guided lamb wave propagation methodology in aerostructures. *Structural Health Monitoring* 0; 0(0): 14759217241249056. DOI:10.1177/14759217241249056. URL https://doi.org/10.1177/14759217241249056. https://doi.org/10.1177/14759217241249056.